Automated 3D geometry segmentation of the healthy and diseased carotid artery in free-hand, probe tracked ultrasound images

Joerik de Ruijter[a)] and Marc van Sambeek
Department of Biomedical Engineering, Eindhoven University of Technology, Eindhoven 5600MB, The Netherlands
Department of Vascular Surgery, Catharina Hospital, Eindhoven 5602ZA, The Netherlands

Frans van de Vosse and Richard Lopata
Department of Biomedical Engineering, Eindhoven University of Technology, Eindhoven 5600MB, The Netherlands

Purpose: Rupture of an arterosclerotic plaque in the carotid artery is a major cause of stroke. Biomechanical analysis of plaques is under development aiming to aid the clinician in the assessment of plaque vulnerability. Patient-specific three-dimensional (3D) geometry assessment of the carotid artery, including the bifurcation, is required as input for these biomechanical models. This requires a high-resolution, 3D, noninvasive imaging modality such as ultrasound (US). In this study, a high-resolution two-dimensional (2D) linear array in combination with a magnetic probe tracking device and automatic segmentation method was used to assess the geometry of the carotid artery. The advantages of using this system over a 3D ultrasound probe are its higher resolution (spatial and temporal) and its larger field of view.

Methods: A slow sweep (v = ± 5 mm/s) was made over the subject's neck so that the full geometry of the bifurcated geometry of the carotid artery is captured. An automated segmentation pipeline was developed. First, the Star-Kalman method was used to approximate the center and size of the vessels for every frame. Images were filtered with a Gaussian high-pass filter before conversion into the 2D monogenic signals, and multiscale asymmetry features were extracted from these data, enhancing low lateral wall-lumen contrast. These images, in combination with the initial ellipse contours, were used for an active deformable contour model to segment the vessel lumen. To segment the lumen–plaque boundary, Otsu's automatic thresholding method was used. Distension of the wall due to the change in blood pressure was removed using a filter approach. Finally, the contours were converted into a 3D hexahedral mesh for a patient-specific solid mechanics model of the complete arterial wall.

Results: The method was tested on 19 healthy volunteers and on 3 patients. The results were compared to manual segmentation performed by three experienced observers. Results showed an average Hausdorff distance of 0.86 mm and an average similarity index of 0.91 for the common carotid artery (CCA) and 0.88 for the internal and external carotid artery. For the total algorithm, the success rate was 89%, in 4 out of 38 datasets the ICA and ECA were not sufficient visible in the US images. Accurate 3D hexahedral meshes were successfully generated from the segmented images .

Conclusions: With this method, a subject-specific biomechanical model can be constructed directly from a hand-held 2D US measurement, within 10 min, with a minimal user input. The performance of the proposed segmentation algorithm is comparable to or better than algorithms previously described in literature. Moreover, the algorithm is able to segment the CCA, ICA, and ECA including the carotid bifurcation in transverse B-mode images in both healthy and diseased arteries. © *2019 The Authors. Medical Physics published by Wiley Periodicals, Inc. on behalf of American Association of Physicists in Medicine.* [https://doi.org/10.1002/mp.13960]

Key words: automated segmentation, carotid artery bifurcation, geometry assessment, image analysis, ultrasound

1. INTRODUCTION

Stroke is a major cause of invalidity and mortality, affecting more than 1 million persons annually in Europe. Approximately 20–25% of all strokes are caused by rupture of an arterosclerotic plaque in the carotid artery.[1] Arterosclerotic plaques tend to develop in the wall at the vicinity of the carotid artery bifurcation, where the common carotid artery (CCA) splits into the internal and external carotid artery (ICA and

ECA). High peak stresses in the fibrous cap of carotid plaques are related to the rupture risk. To assess stresses in plaques and fibrous cap, biomechanical models can be used, typically built using patient-specific imaging data. Research by Nieuwstadt et al.[2] showed that high sampled three-dimensional (3D) models are required for an accurate calculation of the magnitude of the peak plaque/cap stresses. To obtain a patient-specific geometry of the carotid artery bifurcation, a full 3D view of the region of interest is required, as well as an accurate lumen–wall

segmentation. Modalities such as C omputed tomography (CT) and magnetic resonance (MR) either involve ionizing radiation, high costs, or are not accessible for all patients. Ultrasound has the advantage of noninvasive, high-resolution imaging with the drawbacks of anisotropic image resolution and contrast. The goal of this study is to develop a method to obtain a patient-specific, full 3D and detailed geometry of the carotid bifurcation using ultrasound imaging. This geometry can be used to perform accurate geometrical measurements, or as input for simulations such as finite element solid mechanics models of the wall, computational fluid dynamics, and fluid–structure interaction simulations. For clinical acceptance, this method should require a minimal user input, should be able to cover small variations and details of the geometry, and have sufficient accuracy. Manual segmentation by experienced observers is an alternative, but is known to be a labor intensive task that suffers from high intra- and interobserver variability. However, in

ultrasound, image resolution is anisotropic and contrast suffers from speckle, artifacts, and noise, which makes it difficult to use standard image segmentation techniques. Still, several segmentation methods for ultrasound images have been proposed.

Table I gives an overview of segmentations algorithms that have been developed or used to segment the carotid artery in transverse US images. The first step in automatic segmentation in the transverse view is localization (detection) of the CCA or ICA and ECA. This is often done with manual annotation[5,8] and later with automated methods.[9] In general, the shape of the healthy and diseased carotid cannot be modeled as an ellipse. To find the true lumen/wall border, rather than fit an ellipse/circle, additional steps are required. Instead of using the intensity gradient estimation, several authors used local orientation or phase based methods. One of the first successful implementations for ultrasound imaging was reported in Ref.[21] where they used a phase-based scheme to

TABLE I. A literature overview of segmentation algorithms of transverse ultrasound images of the carotid artery.

Paper	Year	Dimensions	Algorithm	Extra information	Bifurcation	Plaque	No. of images	Probetracking	3D Geometry
Robert[3]	1989	3D	Reconstruct voxel volume	3D geometry from 5 B-mode images	no	no	5 (B-mode images)	magnetic probetracking	yes
Abolmaesumi[4]	2000	2D	Star algorithm	Seed point inside lumen	yes	no	1 (B-mode sequence)	robot controller	yes
Mao[5]	2000	2D	Active contour	Seed point inside lumen	no	no	7 (B-mode images)	no	no
Gill[6]	2000	3D	3D deformable contours	Manually placed balloon.	yes	yes	1 (3DUS)	magnetic probetracking	yes
Guerrero[7]	2007	2D	Star Kalman filter	Seed point inside Lumen	no	no	3 (B-mode sequences)	magnetic probetracking	no
Hamou[8]	2007	2D	Active contour	Seed points inside lumen	no	no	91 (B-mode images)	no	no
Golemati[9]	2007	2D	Hough transform	Detection only	no	no	10 (B-mode sequences)	no	no
Stoitsis[10]	2008	2D	Hough transform + Active contours		no	stenosis	10 (B-mode sequences)	no	no
Wang[11]	2009	2D	Spokes algorithm	Ellipse fit	no	no	38 (B-mode sequences)	no	no
Ukwatta[12]	2011	2D	Level set	Anchor points on the boundary on each slice	no	yes	21 (3DUS)	mechanical stage	no
Ukwatta[13]	2013	3D	Sparse field level set	Anchor points on the boundary on each slice	no	yes	21 (3DUS)	mechanical stage	no
Riha[14]	2013	2D	Viola-jones detector	Detection only	no	yes	971 images (15 subjects)	no	no
Benes[15]	2013	2D	Designed machine vision	Detection only	no	no	16 (B-mode sequences)	no	no
Lorza[16]	2013	2D	Surface graph cuts	Reconstruction of voxel volume	yes	yes	20 (B-mode sequences)	magnetic probetracking	yes
Yeom[17]	2014	3D	Correlation map + ellipse fitting	Carotid artery rat	yes	no	12 (B-mode sequences)	mechanical stage	yes
Narayan[18]	2015	2D+t	Local phase information + speckle estimation	Detection + ellipse fit	no	no	4 (B-mode sequences)	no	no
Smistad[19]	2016	2D	Deep convolutional network	Detection	yes	no	2 (B-mode sequences)	no	no
Narayan[20]	2017	2D	Feature assymetry + eccentricity		no	no	971 images[14]	no	no

detect acoustic boundaries in echocardiographic image sequences. Aforementioned segmentation techniques are all based on B-mode images or videos. Instead of using B-mode images, the radio frequency signal can be used for segmenting longitudinal acquisitions of the CCA. An example is the sustain attack low-pass filter, that was developed to detect the vessel wall in longitudinal images.[22]

Still, all these methods were applied or tested on two-dimensional (2D) data whereas the 3D geometry is requires. The 3D geometry of the bifurcated carotid artery can be imaged with a 3D ultrasound probe; however, the spatial and temporal resolution of matrix array probes are currently still inferior to typical linear arrays for 2D imaging, and the field of view (image width) is limited by the size of the transducer and the frequency used, which requires additional steps to obtain a full 3D geometry of the entire carotid artery including the bifurcation. One solution to obtain a high-resolution 3D dataset is mechanical scanning. Here, the movement of a 2D linear array is controlled by a mechanical stage.[17,23,24] The image acquisition is performed in a predefined manner, at fixed spatial positions, so that the dataset is uniformly spaced and there are no missing planes in the acquired volume. For human carotid imaging, this approach is not favorable because of practical issues involving safety and anatomy. Especially the latter requires flexibility to capture the full geometry at the most optimal angle for every patient.

In this study specifically, an approach is introduced and its performance investigated, that allows automatic segmentation of the entire CCA, including the bifurcation, ECA, and ICA. Rather than using a 3D ultrasound probe, the high spatial and temporal resolution of 2D ultrasound are used in combination with a magnetic probe tracking device. By making a ±8 cm sweep over the neck of the patient, the complete geometry of the common, external, and internal carotid artery can be captured, including a possible plaque. This approach requires an automatic segmentation and tracking algorithm of transverse US images covering the full range of the bifurcated carotid artery, including the low contrast images of the ICA and ECA. A segmentation algorithm was developed which only requires two seeds in the first frame. The method was validated in a group of healthy volunteers and compared to manual segmentation by trained observers, and was demonstrated in several patients.

The main contributions of this study are a complete framework to create a full 3D geometry of the healthy and diseased carotid artery using a free-hand US, including the bifurcation and possible plaque. This framework enables large area measurements with robust automatic segmentation, temporal and spatial filtering techniques, and meshing. Compared to similar work,[6,16] our method shows a high level of robustness, and obtains a higher resolution and more accurate geometry. Previous works[12,13] showed 3D lumen–intima and media/adventitia segmentation using a mechanical stage; however they required seed points in every frame. Their work was focused on monitor treatment response, whereas this study focuses on geometry reconstruction for biomechanical modeling, which

requires the larger geometries, ICA and ECA, and the geometry at constant pressure.

2. MATERIALS AND METHODS

2.A. Population

Nineteen healthy volunteers aged between 18 and 30 yr and three patients with severe stenosis were included in this study. All subjects gave informed consent prior to the measurements and are not using any type of cardiac support devices which could be disturbed by the magnetic field of the probe tracking device. This research was granted ethical approval from the ethics committee of the local hospital (Catharina Ziekenhuis Eindhoven, NL). All patients and volunteers gave their informed consent.

2.B. Data acquisition

A clinical MylabOne Vascular Ultrasound system (ESAOTE EUROPE, Maastricht, NL) with a linear probe SL3323 (f_c = 7.5 MHz) was used for all data acquisition. This system is attached to a magnetic probe tracking device (CUREFAB CS, Münich, DE). A protocol was designed that included a slow velocity sweep (10–20 s) over the neck, from the distal to proximal part of the right- and left-side carotid. The measurement started distal to the bifurcation, at the position where both the lumen–wall borders of the ICA and ECA are still fully visible in the B-mode image. The sonographer aimed to perform the sweep with a constant speed and capture the entire vessel(s) in a transverse view. The intima–media thickness was measured using the ArtLAB software (ESAOTE EUROPE, Maastricht, NL). Next, the procedure was repeated for the left carotid artery. Before the measurement, the blood pressure of the volunteer was measured using a standard brachial blood pressure cuff. In a first pilot study, 3 patients (2 males and 1 female, age >65 yr) underwent the sonographic exam described in the previous section. All these patients were scheduled for an endarterectomy procedure.

2.C. Vessel tracking

The CUREFAB system grabbed B-mode frames from the video port of the MyLabOne system. For further post-processing, the video data, with a frame rate of 25 Hz, and the corresponding spatial coordinates were extracted from the probe tracking device. To track the position of the vessel in each image a Kalman filter was used, adapted from Ref.[7]. This algorithm was based on the Star-Kalman algorithm from Ref.[4]. The center point of the vessel is selected manually, in the first frame where both the ICA and ECA are visible, rendering user interaction to a minimum. The Star algorithm is used to estimate the lumen–wall border. Along N radii originating from the center point, with angular equally spaced increments of $\Delta\theta = \frac{2\pi}{N}$, a step edge detection function was used to find high probability edge positions.[25] Next, since the

initial shape of the artery can be approached with an ellipse, an ellipse was fitted through the highest probability edge positions. The radius r of the ellipse is given as a function of the angle θ:

$$r(\theta) = \frac{r_a r_b}{\sqrt{r_a^2 cos^2(\theta - \theta_0) + r_b^2 sin^2(\theta - \theta_0)}} \tag{1}$$

where r_a is the semi-major axis of the ellipse given in pixels, r_b is the semi-minor axis given in pixels, and θ_0 is the angle with respect to the x-axis. From frame to frame, the position of the vessel's center will change, due to variations in the geometry and transducer movement. A temporal Kalman filter was used to stabilize ellipse estimates. The fitted ellipse parameters are used as an observation in the Kalman filter. The Kalman state vector X is used to describe the state of the vessel:

$$X = [x_c, y_c, r_a, r_b, \dot{x}_c, \dot{y}_c, \dot{r}_a, \dot{r}_b]^T \tag{2}$$

here, $\dot{x}_c, \dot{y}_c, \dot{r}_a, \dot{r}_b$ are the time derivatives of the ellipse parameters. The angle θ_0 was not considered as a state variable, since in a healthy artery, the shape is close to a circle, the angle θ_0 is than unclear. The state space equations are written as:

$$\begin{cases} X_{i+1} = \mathcal{F}X_i + \zeta_i \\ u_i = \mathcal{C}X_i + \vartheta_i \end{cases} \tag{3}$$

with $\mathcal{F}$ and $\mathcal{C}$ the constant state transition matrix and measurement matrix, given, respectively, by:

$$\mathcal{F} = \begin{bmatrix} I_4 & I_4\Delta t \\ 0_4 & I_4 \end{bmatrix} \qquad \mathcal{C} = [I_4 \quad 0_4] \tag{4}$$

I_n represents a n by n identity matrix and 0_n a n by n zero matrix. Here, u_i is a column containing the ellipse parameters estimated in frame i. ζ_i and ϑ_i are the sequences of white, zero-mean, Gaussian noise, Δt is set to 1. Fig. 1 shows an overview of the tracking and segmentation method.

2.C.1. Centerline correction

Abrupt movements by the sonographer can result in loss of vessel tracking. These movements are registered by the probe tracking device. Instead of solely initiating the Star algorithm on X_{i-1}, the center point is updated by the expected movement of the vessel center, based on the measurement by the probe tracking device. It is assumed that the image plane of frame f_{i-1} is perpendicular to the vessel, and as a consequence the estimated center point $(x_c, y_c)_i^*$, is the intersection with the image plane of the next frame f_i and the outer normal originating from $(x_c, y_c)_{i-1}$. If the distance between the center points $(x_c, y_c)_i^*$ and $(x_c, y_c)_{i-1}$ is greater than five pixels, centerline correction is applied.

2.C.2. Bifurcation

Seeds were placed in the ICA and ECA and each artery was considered separately. Once the ellipses intersect near the bifurcation, the outer eight-shaped contour is used in the next step. Once one of the ellipses encloses the center point of the other ellipse, the ICA and ECA are considered to be merged into the CCA. To determine the initial Kalman parameters for the CCA, an ellipse is fitted through the combined outer (convex hull) contour points of the ICA and ECA.

2.D. Segmentation

To find a more accurate delineation of the lumen–intima boundary, an active contour model is used, initialized with the previously acquired ellipse contours X. This ellipse contour was re-sampled to 100 points using linear interpolation. The active contour model is adapted from Kass et al.[26] The so-called snake energy E_{snake}^* is minimized,

$$E_{snake}^* = \int_0^1 [E_{int}(x(s)) + E_{image}(x(s)) + E_{con}(x(s))]ds \tag{5}$$

with $x(s)=(u(s),v(s))$, the image coordinates and E_{image} is the total image energy. This energy term moves the snake towards line and edge features in the image. The internal energy E_{int} prevents the snake from bending and stretching and basically keeps the contour smooth. E_{con} is the external constraint energy, which is in our model a balloon energy, "pushing" the contour to the vessel wall. To ensure a robust segmentation, instead of using the original B-mode image, the image is preprocessed (Fig. 2). First, image sharpening was performed using a Gaussian high-pass filter in the frequency domain, which improves visibility of the wall structures.[27] The transfer function of the Gaussian high-pass filter is given by:

$$H(u, v) = 1 - \exp\left(-\frac{D(u, v)^2}{2D_0^2}\right) \tag{6}$$

where D_0 is the cut-off frequency (unit: pixel^{-1}) and $D(u,v)$ the distance from the origin of the Fourier Transform for an N by M image is given by:

$$D(u, v) = \sqrt{\left(u - \frac{M}{2}\right)^2 + \left(v - \frac{N}{2}\right)^2} \tag{7}$$

Next the 2D monogenic signal is calculated using the 2D even log-Gabor filter[28]:

$$G_{even}(\omega) = \exp\left(-\frac{(\log(\frac{abs(\omega)}{\omega_0}))^2}{2(\log(\sigma_0))^2}\right) \tag{8}$$

here, ω is the two-dimensional frequency in the 2D Fourier transform of the original image. After filtering the monogenic signal can be written as:

$$f_m(x) = \begin{bmatrix} f_e(x) \\ f_{o1}(x) \\ f_{o2}(x) \end{bmatrix} \tag{9}$$

The 2D monogenic signal consists of one even component f_e and two odd components f_{o1} and f_{o2}, which can be combined to one odd part:
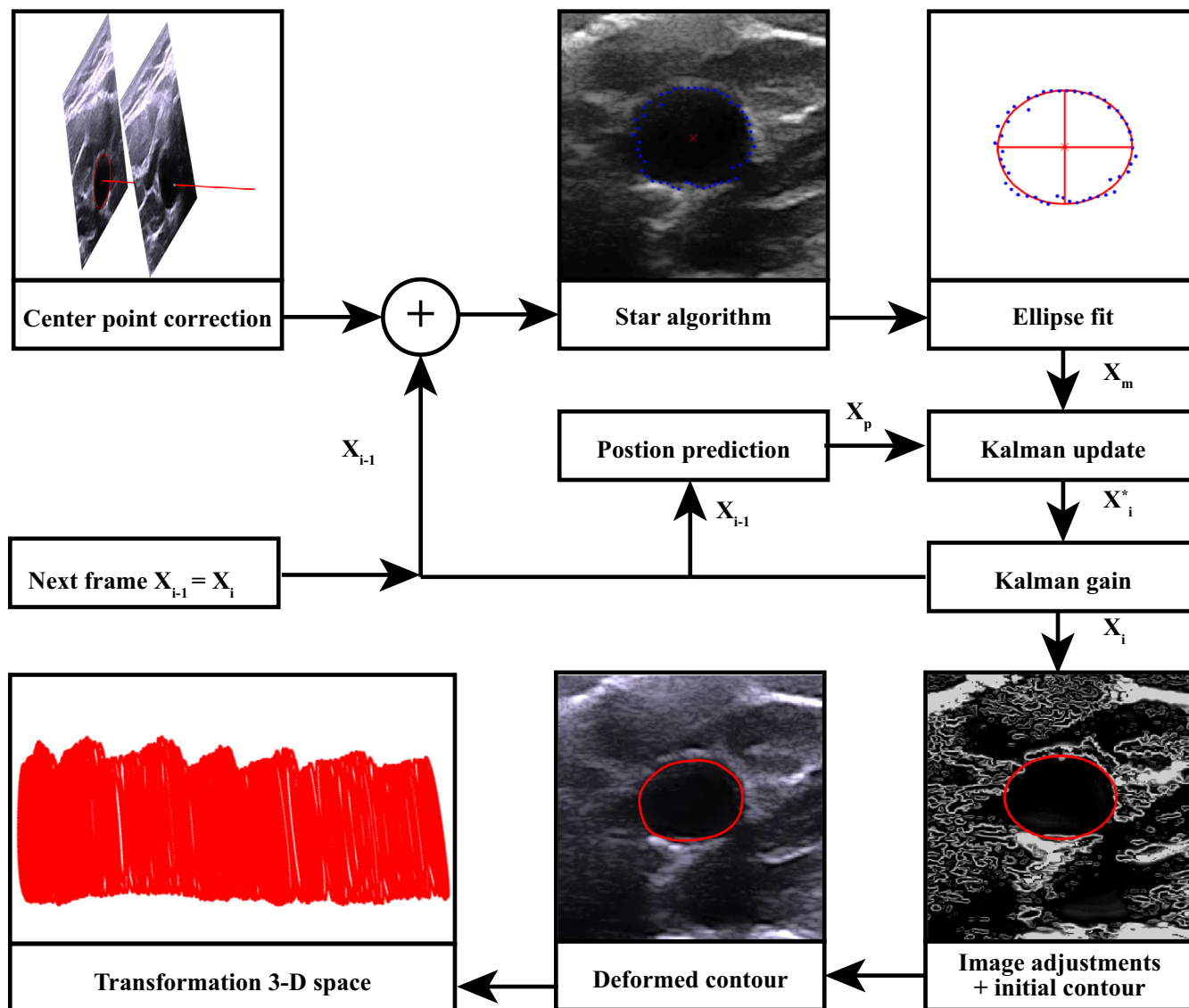
FIG. 1. Overview of the tracking and segmentation algorithm.

$$f_o(\boldsymbol{x}) = \sqrt{f_{o1}(\boldsymbol{x})^2 + f_{o2}(\boldsymbol{x})^2} \qquad (10)$$

To detect edges, the Kovesi's feature asymmetry measure (FA) was calculated based on the monogenic signal[29]:

$$FA(\boldsymbol{x}) = \sum_i \frac{\lfloor |f_{o,\lambda_i}(\boldsymbol{x})| - |f_{e,\lambda_i}(\boldsymbol{x})| - T \rfloor}{A_{\lambda_i}(\boldsymbol{x}) + \epsilon} \qquad (11)$$

here, λ is a set of wavelengths of the band-pass filter used to calculate the monogenic signal. $A(\boldsymbol{x})$ is the amplitude of the combined odd component with the even component. The notation $\lfloor . \rfloor$ means that every negative value is replaced with a zero, whereas the factor ε prevents a division by zero. T, a scale specific noise threshold, is set to 0.18 (adapted from Bridge[28]). After normalizing $FA(\boldsymbol{x})$, every value lies in the range $0 < FA(\boldsymbol{x}) < 1$, where a value close to 1 corresponds with wall structures. To avoid that the snake is located between two wall borders, intensity thresholding of the

original B-mode image is used. The pixels with a higher intensity than the 80th percentile of the B-mode image, most likely wall structures, are filled with the maximum pixel intensity.

2.E. Plaque segmentation

In arteries with a plaque present, the ellipse that was estimated using the Star-Kalman tracking algorithm is not suitable as initial guess for the snake. To extract the lumen boundary in arteries with plaque, we propose to use Otsu's automatic thresholding method,[30] applied within the ellipse found with the Star-Kalman algorithm to detect the lumen boundary. First the original US image was smoothened using a Gaussian smoothing, so that the resulting boundaries are less sharp. A mask of the detected Kalman contours was used for Otsu's automatic thresholding algorithm with three
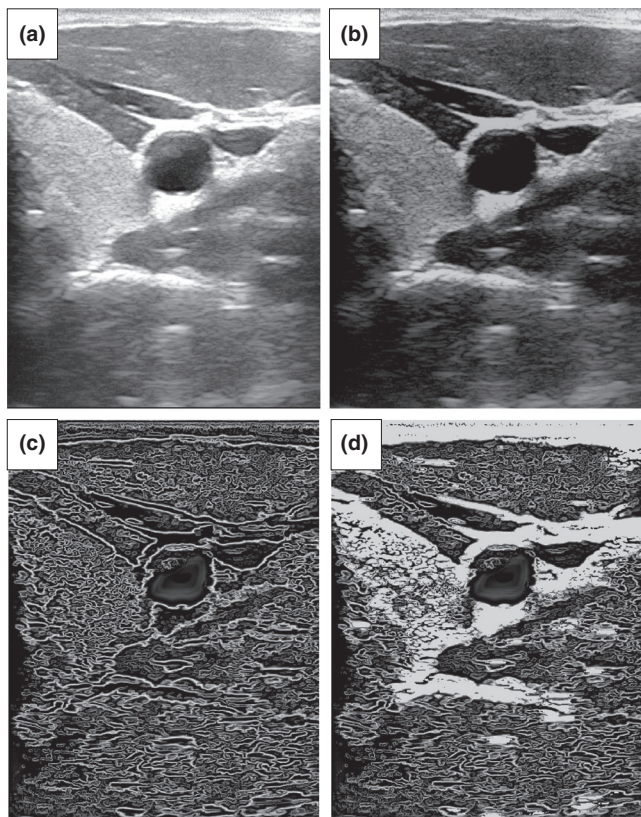
FIG. 2. (a) Original B-mode image, (b) image sharpening using a high-pass Gaussian filter, (c) feature asymmetry image, and (d) final image used for deformable contour model deployment, that is, feature asymmetry plus thresholding.

classes, see Fig. 3 (LEFT). Next, the boundaries were extracted from the contour around class with the lowest gray values, which represent the lumen, see Fig. 3.
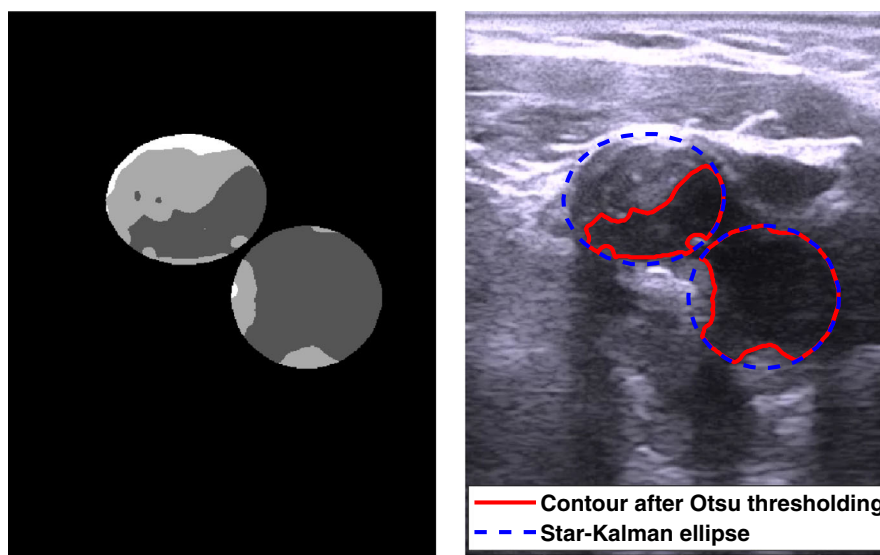
2.F. Temporal filtering

A major drawback of all these sweep methods is the presence of natural geometrical changes (distension) caused by the pulsation of the wall, that is, wall motion induced by blood pressure variations during the cardiac cycle. These variations can be nonuniform over the angle θ, possibly caused by either irregular distribution of the force acting on the arterial wall, nonuniform flow patterns, and/or differences in mechanical properties of the wall and the surrounding tissue. Second, variations in external forces can cause a rigid motion of the artery. These variations can be caused by the probe pressure, breathing, swallowing, or other types of body motion. During the measurements, the sonographer and the volunteer aimed to minimize these external disturbances. Before filtering, the centerline is corrected for rigid motion of the artery due to the heartbeat, by using the center of mass of every end-diastolic frame. These values are used to correct the centerline for the other frames in time using linear interpolation. The corrected centerline x_c can be described as a combination of the interpolated end-diastolic centerline and the center of mass of the segmented contours denoted by x_m.

$$x_c = (1 - w_c) \cdot x_m + w_c \cdot x_{dc} \tag{12}$$

here w_c is a weight factor and x_{dc} are the pixel coordinates of the diastolic centerline. The distension of the arterial wall due to the changes in arterial blood pressure p_{art} is clearly visible in the segmented contours (Fig. 4). In the proposed method, the contours are corrected for the change in arterial blood pressure, so that the geometry is equal to its state at the mean arterial pressure p_{map}. The heart rate (frequency f_{hr} in Hz) is detected using the Fourier transform of the segmented area of each slice over time. The highest peak within the physical range of the heart rate is detected in the power-density spectrum. Since the heartbeat causes a periodic signal over time,
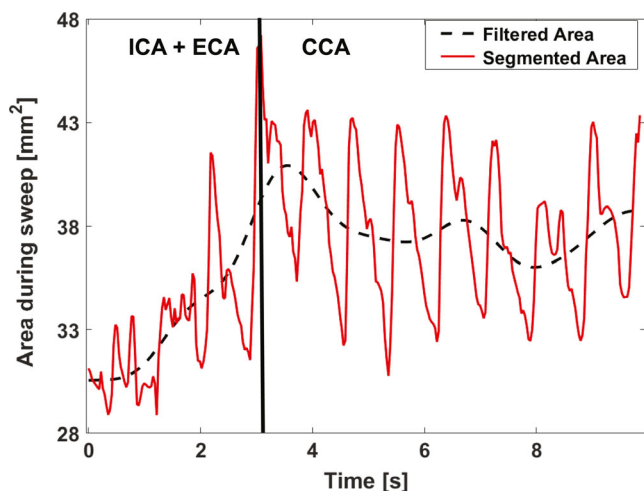

FIG. 3. Example of segmentation of the lumen boundary in presence of plaque tissue. LEFT: Otsu thresholding was applied to the gray value data within the Star-Kalman ellipse. RIGHT: The original US image with the Star-Kalman ellipse (blue) and the detected lumen boundary (red).

FIG. 4. Example of the segmented area of each contour (red) in [mm^2] over time [s], the dotted line is the area of the contours after temporal filtering. The vertical black line represents the position of the bifurcation, on the left of that line the area of the internal and external carotid artery are combined. [Color figure can be viewed at wileyonlinelibrary.com]

it can be removed in the frequency domain using a stop-band or "notch" filter centered around f_{hr}. This filtering could be performed in the area-frequency-domain, however, nonuniform radial displacements were observed. So, it is more accurate to filter the area-time signal in the radius-frequency domain. Next, all contours were converted into cylindrical coordinates, see Fig. 5. An uniform time — θ grid was created using linear interpolation. For every θ, the r-t curve was transformed to the Fourier domain, using the Fast Fourier Transform (FFT). Instead of a stop-band or 'notch' filter, a low-pass filter with cut-off frequency f_{hr} was used, since high frequency variations in the radius are most likely caused by small segmentation errors.

2.G. Meshing

For volume rendering, the estimated carotid geometry needs to be transformed into a 3D mesh. After temporal filtering, nonoverlapping contours/frames are selected,
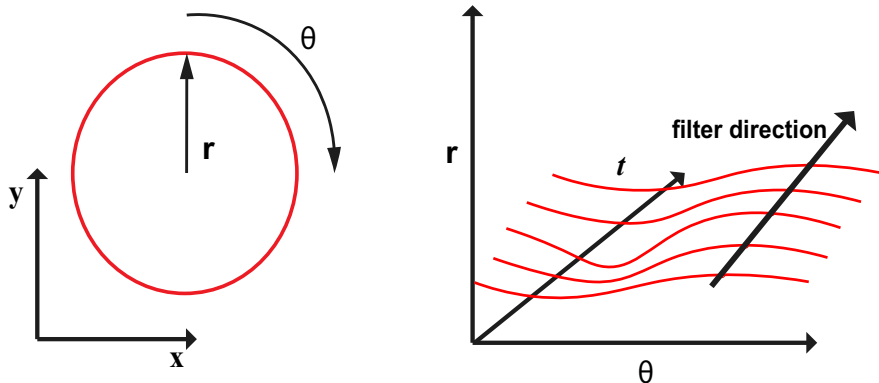
depending on the desired mesh density in longitudinal direction. To mesh the bifurcation, a module from the MATLAB-based Gibbon toolbox was adapted.[31] The triangulated mesh is smoothed using curvature flow smoothing.[32] The steps from unfiltered contours to smooth surface mesh are visualized in Fig. 6.

2.G.1. Segmentation evaluation metrics

Three expert observers manually traced the lumen–wall border of six to eight frames per acquisition, three distal from the bifurcation, and four proximal to the bifurcation, see Fig. 7. In the first frame, the center of the ICA and ECA was annotated, to make sure the observers were able to find the right arteries in the US image. The automated segmented contours were compared with manual contours using different metric proposed in literature. The Haussdorf distance (H_D) shows the maximal shortest distance between two contours.[33]

The dice similarity coefficient (DSC), also known as the Similarity Index (S_I), can be used as spatial measure that quantifies the overlap between two areas.

$$S_I = \frac{2(\mathcal{A} \cap \mathcal{B})}{\mathcal{A} + \mathcal{B}} \tag{13}$$

here, $\mathcal{A}$ and $\mathcal{B}$ are the areas of contours A and B. If $S_I = 0$, there is no overlap between $\mathcal{A}$ and $\mathcal{B}$, whereas for $S_I = 1$ the contours are identical. Other area-based metrics are the so-called sensitivity (S_E) and accuracy (A_C), which are defined as:

$$S_E = \frac{T_P}{\mathcal{A}} = \frac{T_P}{F_N + T_P} \tag{14}$$

$$A_C = 1 - \frac{F_P + F_N}{\mathcal{A}} \tag{15}$$

here, $\mathcal{A}$ is the "true" area, in this study the area of the manual segmented contour. T_P is true-positive area, F_P the false-positive area and F_N the false-negative area, all based on the "true" contour A and the automatic segmented contour B.[5]

FIG. 5. Contours are transformed to polar coordinates ($r-\theta$). A low-pass filter was performed in the r - t - direction. [Color figure can be viewed at wileyonline library.com]
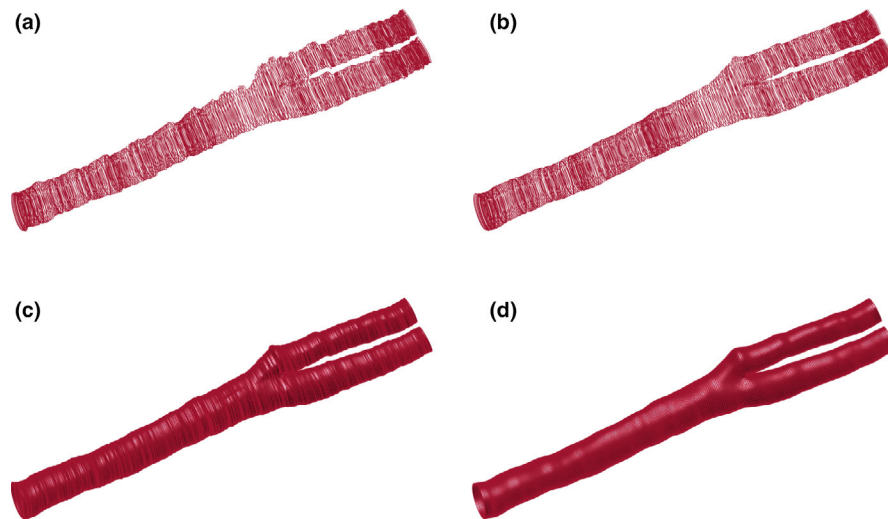
FIG. 6.   (a) Contours obtained from the automatic segmentation algorithm, (b) contours after temporal filtering, (c) surface mesh obtained from the selected contours, and (d) surface mesh after curvature flow smoothing. [Color figure can be viewed at wileyonlinelibrary.com]
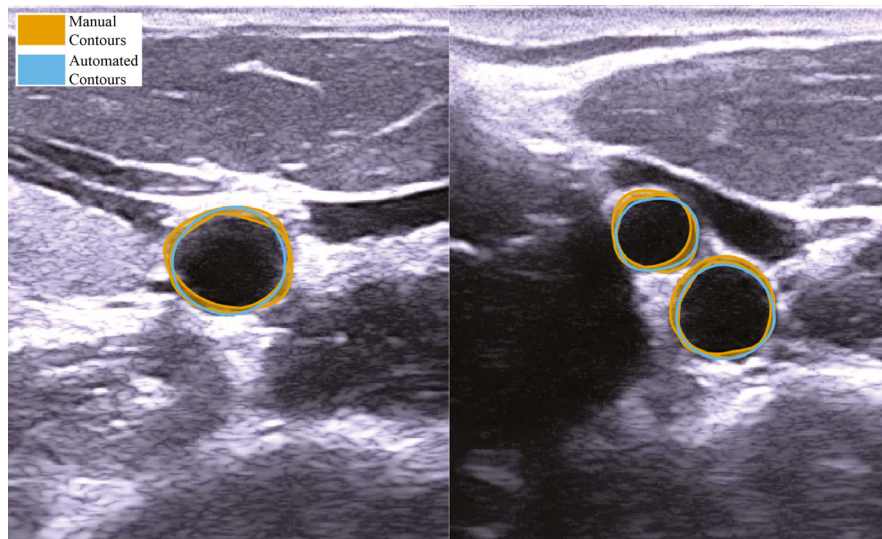

FIG. 7.   LEFT: Common carotid artery, RIGHT: Internal and external carotid artery with the combined manual segmented contours (red) and segmentation algorithm contours (blue).

3. RESULTS

The proposed method was tested on 41 acquisitions of 19 different volunteers and three patients, that is, both the left and right carotid artery in the healthy volunteers, and the stenosed artery in the patients, respectively. The average sweep speed was 5.4 ± 1.2 mm/s. Four measurements were excluded since the ICA and ECA were not visible/detectable by human observers. This can be caused by bad image quality or the inability to create a proper view that includes both the ICA and ECA. Each observer segmented 149 frames for the CCA and 93 frames for ICA and ECA of the healthy volunteer datasets. Overall, the observers tend to be more in agreement in terms of the lumen–wall borders in axial direction.

For both, volunteer and patient data, the tracking algorithm was used. However, for segmentation, the data were categorized as images with and without plaque. Images without plaque were segmented using the algorithm described in Section 2.D and images with plaque with the algorithm described in Section 2.E. Figures 8 and 9 shows the automated segmented area vs manual segmented area of each observer. For bigger areas near the bifurcation, the algorithm tends to underestimate the total surface. Observer 2 (44 mm^2) and 3 (45 mm^2) segmented on average a larger CCA area compared to observer 1 (41 mm^2) and the algorithm (40 mm^2). Bland–Altman plots (Figs. 8 and 9) show a mean difference of -3.2 mm^2 for the CCA and -1.0 mm^2. This underestimation of the area is also confirmed by the regression of $y = 0.91x$.

Figure 10 shows box-and-whisker plots of the similarity index, Hausdorff distance, accuracy, and sensitivity for each observer separately. The box-and-whisker plots are generated
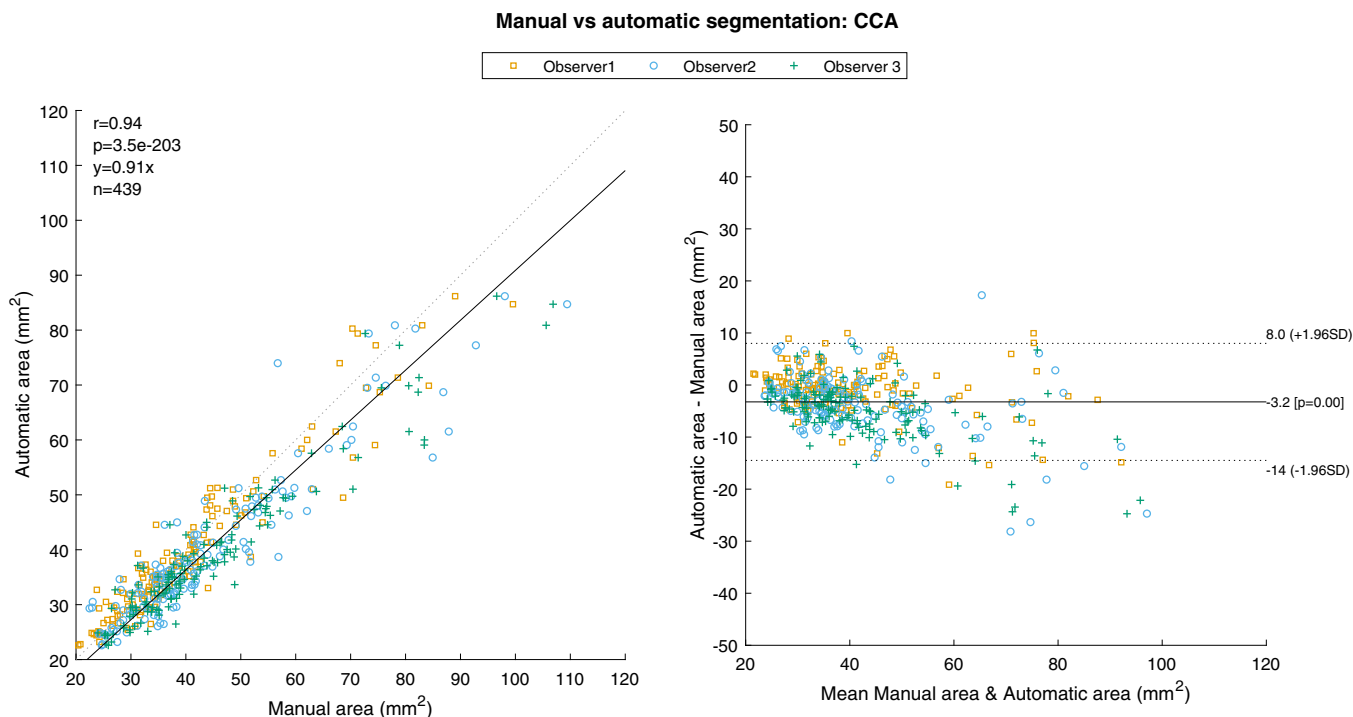
Manual vs automatic segmentation: CCA

FIG. 8. Comparison between manual and automated segmented common carotid artery area [mm^2]. The left panel shows the regression (forced to intersect the origin) results and the right panel shows the Bland–Altman plot. The difference is $-3.2\,mm^2$, r and p are the Pearson r-value and correlation P-value, respectively. [Color figure can be viewed at wileyonlinelibrary.com]

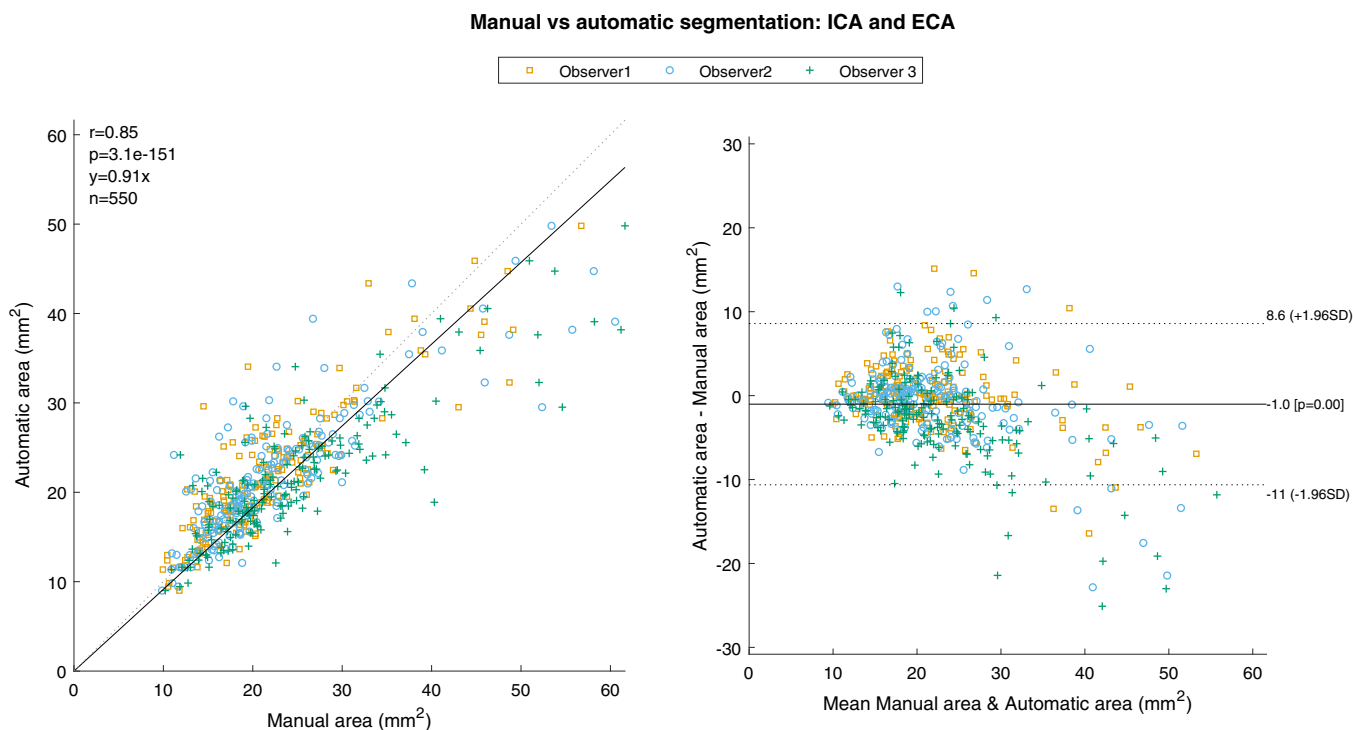**Manual vs automatic segmentation: ICA and ECA**

FIG. 9. Comparison between manual and automated segmented internal and external carotid artery area [mm^2]. The left panel shows the regression results (forced to intersect the origin) and the right panel shows the Bland–Altman plot. The difference is $-1.0\,mm^2$, r and p are the Pearson r-value and correlation P-value, respectively. [Color figure can be viewed at wileyonlinelibrary.com]

for two distinct parts: from proximal CCA to the bifurcation (ICA & ECA) and the volume ranging from the most distal image to the bifurcation (CCA). The segmentation of the CCA is more accurate than the automatic segmentation of the ICA and ECA, as shown by all metrics with Similarity indexes between 0.89 and 0.94 (CCA) vs 0.85 and 0.91 (ICA/ECA)
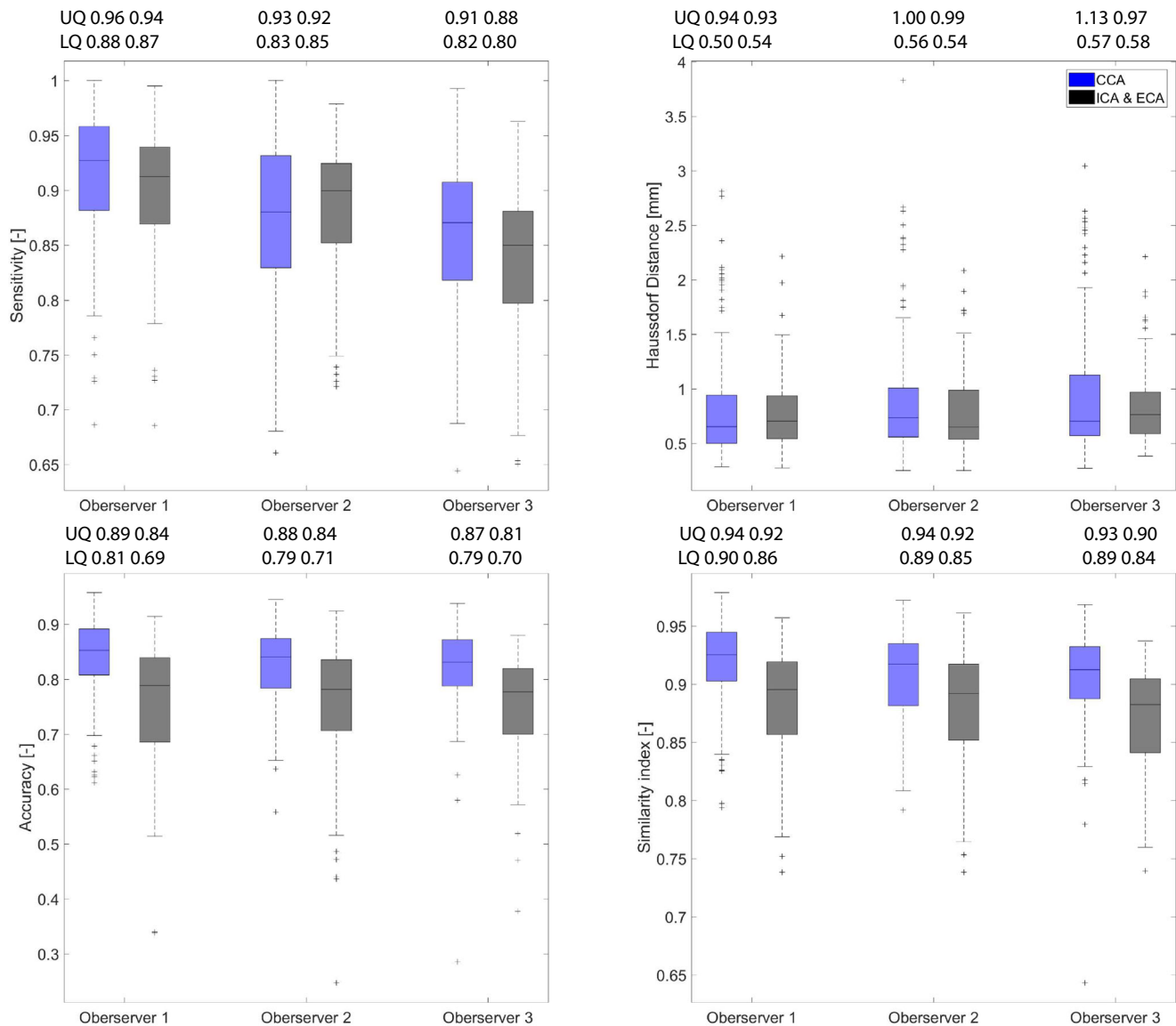
Fig. 10.   Box-and-whiskers plots of the quality metrics for automated segmentation. There are 149 manual segmented contours per observer for common carotid artery and 93 for internal and external carotid artery. [Color figure can be viewed at wileyonlinelibrary.com]

and sensitivity values of 0.84–0.94 (CCA) vs 0.83–0.92 (ICA/ECA). In Table II all metrics are reported for the CCA and ICA/ECA regions, including their median and the lower and upper quartiles. In Fig. 11, 24 geometries after removal of the heartbeat and filtering are displayed. Ten geometries were not displayed, since there were not enough frames of the ICA/ECA available in the sweep, which impedes determination of the heartbeat-free geometry. The length of acquisitions varies between 37.7 and 95.9 mm. In the "longer" acquisitions, some movement of the patient was observed.

Figure 12 shows segmentation and geometry construction of three patient measurements. The contours displayed in red, that is, the stenosed areas, are found using the algorithm described in Section 2.E, whereas the blue contours were detected using the Star-Kalman algorithm (see Section 2.C). The panels in the right show the obtained geometries of the lumen–wall or plaque boundary. The

stenosis, indicated with a black arrow, are visible at different locations: in the ICA (Patient A and B) and proximal to the bifurcation (Patient B and C). Patients B has a severe stenosis in the CCA, whereas the degree of stenosis in patient C is mild (50–70%).

4. DISCUSSION

In this study, we presented a complete and automated framework, that was capable of assessing the total geometry of the CCA, including the bifurcation, ICA and ECA, and possible plaque. The use of 2D ultrasound in combination with probe tracking provides the desired 3D geometry for stenosis evaluation, mechanical modeling purposes, etc., while exploiting the higher resolution and low cost of 2D ultrasound. Due to its limited user input, this framework enables to create a 3D directly from the measurement, within

TABLE II. Manual vs automated segmentation, the manual segmentations of all three observers are combined.

	CCA (iqr)	CCA (mean)	ICA & ECA (iqr)	ICA & ECA (mean)
H_D [mm]	0.68 (1.02–0.53)	0.86	0.71 (0.96–0.55)	0.80
S_I [-]	0.92 (0.89–0.94)	0.91	0.89 (0.85–0.91)	0.88
S_E [-]	0.89 (0.84–0.94)	0.88	0.88 (0.83–0.92)	0.87
A_C [-]	0.84 (0.80–0.88)	0.83	0.78 (0.70–0.83)	0.76

For the common carotid artery (CCA) and the internal and external carotid artery (ICA/ECA), the median including the lower and upper quartiles are reported. The Hausdorff distance (H_D), the similarity index (S_I), the sensitivity (S_E), and the accuracy (A_C) are reported.

± 10 min on a standard personal computer. The proposed method can also be used for the geometry reconstruction of other "large" superficial arteries such as the femoral artery and the brachial artery, where it is possible to achieve similar images with sufficient contrast/resolution. The proposed segmentation algorithm combines three different segmentation techniques to solve a number of common problems in segmentation of carotid arteries in transverse US images, by exploiting the advantages of each technique. First of all, localization of the arteries, especially the ICA and ECA is challenging. Benes et al.[15] shows localization of the CCA with success rate of 82.7%, and state of the art work[20] shows a sensitivity of 98.1% on a public database, but the localization success rate is unclear. However, the performance of localization algorithms for the ICA and ECA in humans has not been reported in literature so far, only on rat's carotid arteries[17].

In our proposed method, the tracking algorithm provides a reliable estimate for the position and size of the ECA, ICA and CCA. By coupling the Star-Kalman algorithm to probe tracking information, the algorithm is able to also correct for unpredictable probe movements by the sonographer. Most artery detection algorithms rely on an ellipse/circle fit.[7,9,41] To find the true lumen–intima/wall border active contour algorithms (snakes) can be used.[5,8,10] However, snake algorithms heavily rely on the initial contour, which is solved in this study by using the tracking algorithm results. Moreover, snakes are intensity or intensity gradient based and there is less signal/reflection on the left and right side of the arterial wall due to the physics of ultrasound propagation. As a result, the snake tends to cross the actual borders and "leaks" out of the vessel. Therefore, we propose to use the monogenic signal analytically derived by Felsberg and Sommer.[34] The advantage of using the monogenic signal over the B-mode image, is the high contrast between the lumen and the wall, whereas in the B-mode image there is almost no distinction.

In 3D freehand US imaging, the images are captured on arbitrary positions, controlled manually by the operator.[3] This gives the freedom to acquire the optimal views and move the transducer over the irregular surface of a human neck. Several techniques have been proposed: acoustic, optical, and magnetic probe tracking.[3,35,37] Fenster and Downey[38] used
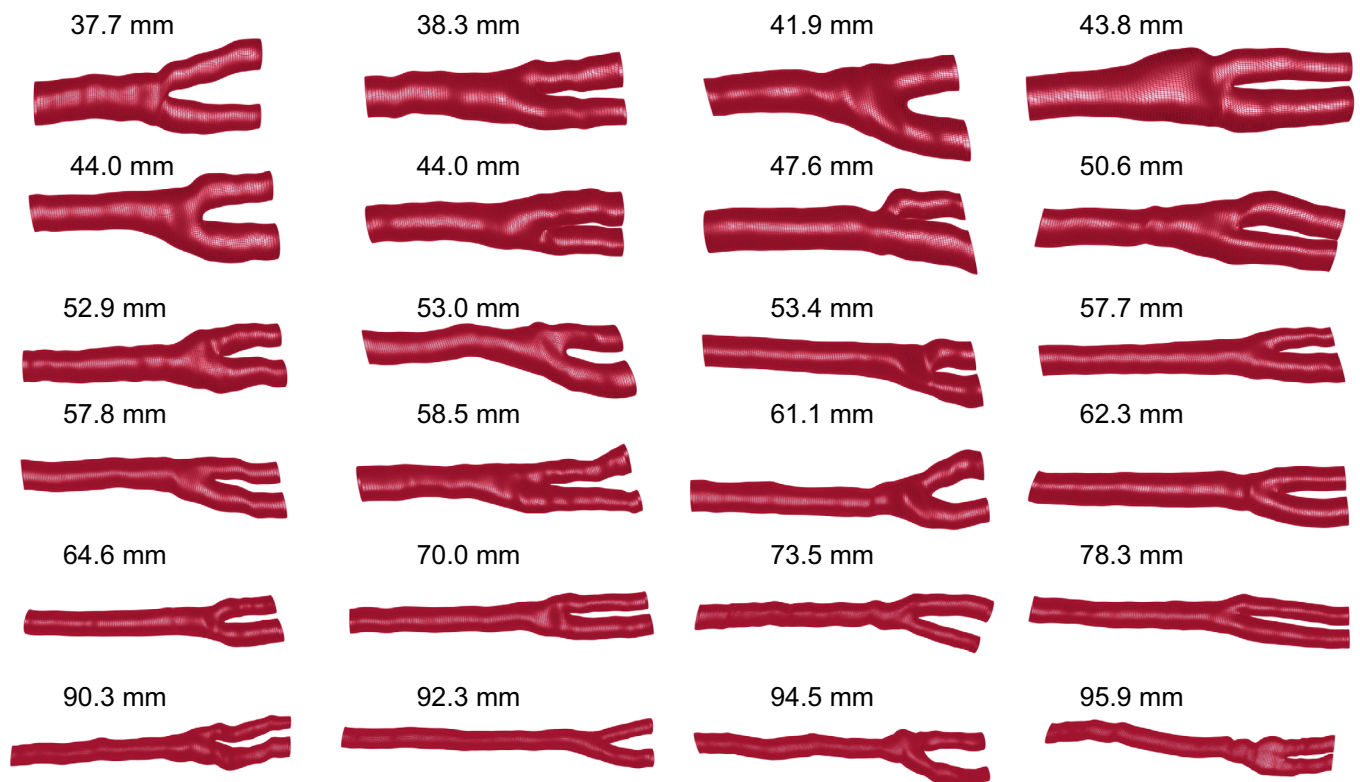

FIG. 11. Twenty-four geometries of healthy volunteers increasing in size. The total length of each geometry is given in millimeters. [Color figure can be viewed at wileyonlinelibrary.com]
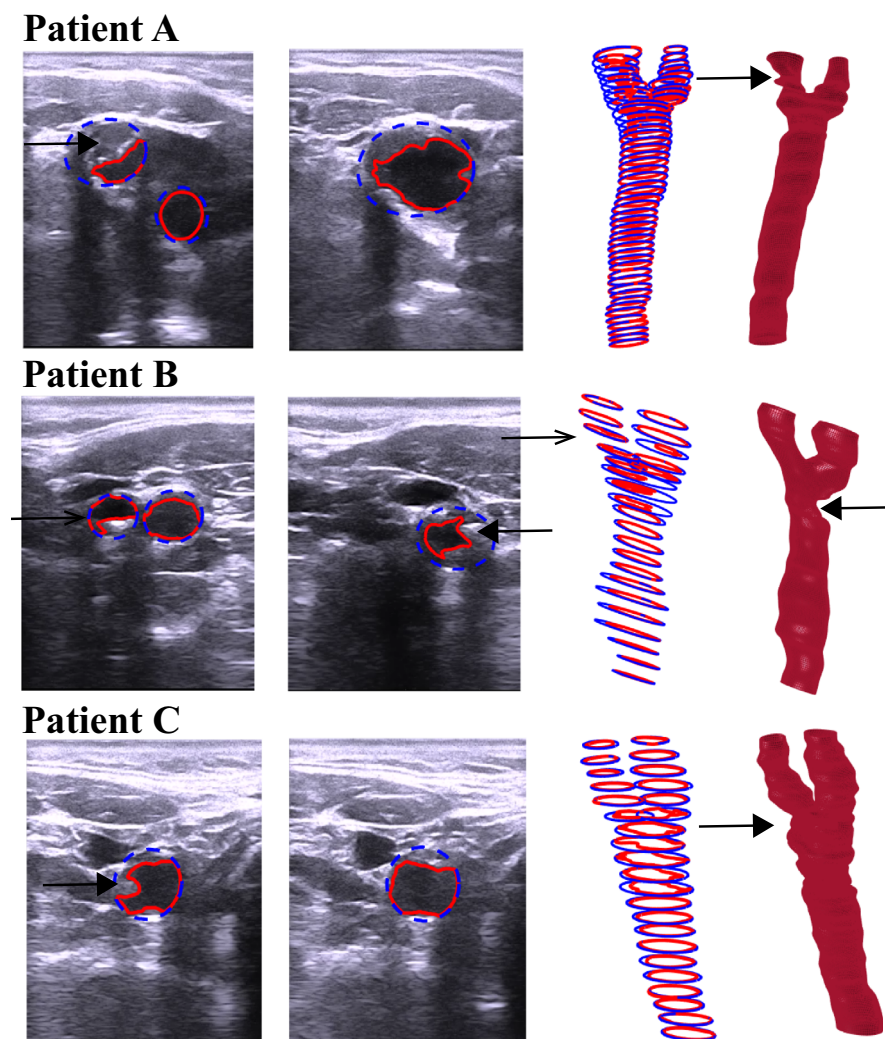
Patient A

Patient B

Patient C

FIG. 12. Segmentation and three-dimensional geometry of three patient datasets. For each patient, two US images show the lumen–wall/plaque boundary in red and the Star-Kalman contours in blue. The geometries on the right show the lumen-wall/plaque meshes after curvature flow smoothing, see Section 2.G. The arrows indicate stenosed locations, in the US images and geometry.

magnetic field sensor tracking to create a 3D volume of the carotid, a balloon model was manually placed to initialize a 3D discrete dynamic contour algorithm to segment the vessel's lumen. Carvalho et al.[39] developed an algorithm to track the carotid artery lumen centerline, but did not perform segmentation of the lumen. Instead of using B-mode, Power Doppler can be a using in combination with magnetic probe tracking to grade the stenosis of the internal carotid artery,[40] which was not considered in our study.

The performance of the algorithm was evaluated using the quality metrics described in Section 2.G.1 and were compared to literature. An average similarity index of 0.91 was found, which is significantly higher than 0.83 ± 0.07 (95% confidence interval) reported by Wang et al.[11] and comparable with the results obtained by Smistad et al.[19] Moreover, the mean Hausdorff distance of our proposed algorithm is lower: 0.86 mm compared to 1.05 ± 0.15 mm. The Dice coefficient, similar to S_I, of 0.88 ± 0.04 and 0.88 ± 0.02 reported by Narayan et al.[20] is slightly lower than the S_I of the method

proposed. Sensitivity of 0.88 for the segmentation of the CCA is a slight improvement compared to the 0.82–0.84 reported by Golemati et al.[9] and 0.82–0.85 by Stoitsis et al.,[10] although those methods were fully automated and applied to the CCA region only. The specificity, similar to our definition of S_E, of 0.836–0.908 reported in study of Narayan et al.[20] is comparable to 0.88 found in this study. Visible inspection of the delineations by the plaque segmentation algorithm reveal the performance of the method. However, due to limited patient data, no extensive comparison with manual segmentation was performed.

Lorza et al.[16] shows a 3D geometry reconstruction based on reconstructed voxel volume data. They report an average Dice coefficient of 0.84 for healthy volunteers compared to 0.91 in our study. A disadvantage of free-hand imaging is that the acquired volume is irregularly spaced and might contain regions that lack image data. Hence, voxel-based methods using free-hand 2D ultrasound will lose resolution when reconstruction the voxel volume, however, the method proposed does not suffer from this issue, since our method does

not rely on a reconstructed volume. In our method the pixel-size is 0.0742 *mm* compared to their voxel-size of 0.21 *mm*, both for a depth of 4 *cm*.

4.A. Limitations

A total of 41 acquisitions were analyzed. Due to bad visibility of the ICA and ECA four datasets were excludes, since the goal of this study and methodology was to reconstruct the complete carotid geometry. Moreover, the geometries of ten datasets were not shown, despite successful segmentation and tracking. This was due to the fact that the number of frames containing the ICA and ECA was limited, since at least 30 frames are required for the Fourier-based heartbeat removal. This can be solved by improved instructions to the sonographer and lowering the sweep velocity. This and other probe tracking methods can only be successful if the subject can minimize body movement, breathing, and swallowing. It is important that the subject lies in a comfortable position and is instructed to breathing quietly and avoid swallowing. Visual inspection shows that the geometries are realistic, however some motion artifact are seen. Solutions would be a brace to restrict body movement, or the inclusion of a second (magnetic) sensor directly to the subject's neck to correct for body movement. Validation of the geometries could be done using MRI or CTA, but these data are not available for volunteers for the obvious reasons. The current methodology requires two seeds in the first frame, in the ICA and ECA. The exact location of the seed does not influence the final results, since the algorithm will find the correct lumen–wall boundary within five frames, although the first frames should be excluded for the final geometry render. Furthermore, the method is a processing pipeline that consists of several modules, each with multiple parameters. A sensitivity analyses should be performed to identify the most important parameters, whereas tuning those parameters (e.g. with machine learning techniques) could help improve the performance in future studies.

4.B. Future work

In future work, the patient study will be extended. These geometries will have more irregularities as was seen in the cases included in this study. Additional challenges will be the presence of one or multiple stenoses, and the presence of calcifications, which will cause shadowing in the B-mode image. A possible solution is to combine multiple sweeps to obtain sufficient contrast over the full length of the carotid artery. Deep-learning approaches are a promising tool for medical image segmentation.[41] developed a deep convolutional neural network that was able to classify blood vessels in B-mode ultrasound images. Such a technique has not been used yet to find the exact lumen–wall borders in the full carotid geometry. An extension of our current work with deep learning could aid in tackling the aforementioned challenges typically encountered in patient datasets.

5. CONCLUSIONS

In conclusion, a method was developed to generate an accurate, high resolution, 3D geometry of the carotid artery and bifurcation directly from a free-hand 2D US measurement. The automatic segmentation algorithm, developed to segment the healthy and diseased carotid artery with a minimal user input, revealed an average similarity index of 0.91 in the CCA, an average similarity index of 0.88 in the ICA and ECA of healthy volunteers. Moreover, its ability to assess the geometry in diseased carotid arteries was demonstrated. Future studies will be conducted to validate the performance in providing patient-specific input data for biomechanical analysis of plaques.

CONFLICT OF INTEREST

The authors have no conflict to disclose.

a)Author to whom correspondence should be addressed. Electronic mail: j.d.ruijter@tue.nl.

REFERENCES

1. Petty GW, Brown RD, Whisnant JP, Sicks JD, Fallon WMO, Wiebers DO. A population-based study of incidence and risk factors. *Stroke*. 1999:2513–2516.
2. Nieuwstadt HA, Akyildiz AC, Speelman L, et al. The influence of axial image resolution on atherosclerotic plaque stress computations. *J Biomech*. 2013;46:689–695.
3. Robert H, Blankenhorn DH, Howard J. Computer-generated 3D ultrasound images of the carotid artery; 1989:21–26.
4. Abolmaesumi P, Salcudean SE, Zhu WH, Sirouspour MR, DiMaio SP. Image-guided control of a robot for medical ultrasound. *IEEE Trans Robot Autom*. 2002;18:11–23.
5. Mao F, Gill J, Downey D, Fenster A. Segmentation of carotid artery in ultrasound images: method development and evaluation technique. *Med Phys*. 2000;27:1961–1970.
6. Gill JD, Ladak HM, Steinman DA, Fenster A. Accuracy and variability assessment of a semiautomatic technique for segmentation of the carotid arteries from three-dimensional ultrasound images. *Med Phys*. 2000;27:1333–1342.
7. Guerrero J, Salcudean SE, McEwen JA, Masri BA, Nicolaou S Real-time vessel segmentation and tracking for ultrasound imaging applications. *IEEE Trans Med Imaging*. 2007;26:1079–1090.
8. Hamou AK, Osman S, El-Sakka MR. Carotid ultrasound segmentation using DP active contours. In: *Image Analysis and Recognition*. Berlin: Springer; 2007:961–971.
9. Golemati S, Stoitsis J, Sifakis EG, Balkizas T, Nikita KS. Using the hough transform to segment ultrasound images of longitudinal and transverse sections of the carotid artery. *Ultrasound Med Biol*. 2007;33:1918–1932.
10. Stoitsis J, Golemati S, Kendros S, Nikita KS. Automated detection of the carotid artery wall in B-mode ultrasound images using active contours initialized by the Hough transform. 2008 30th Annual International Conference of the IEEE Engineering in Medicine and Biology Society; 2008:3146–3149.
11. Wang DC, Klatzky R, Wu B, Weller G, Sampson AR, Stetten GD. Fully automated common carotid artery and internal jugular vein identification

and tracking using B-mode ultrasound. *IEEE Trans Biomed Eng*. 2009;56:1691–1699.

12. Ukwatta E, Awad J, Ward AD, et al. Three-dimensional ultrasound of carotid atherosclerosis: semiautomated segmentation using a level set-based method. *Med Phys*. 2011;38:2479–2493.

13. Ukwatta E, Yuan J, Buchanan D, et al. Three-dimensional segmentation of three-dimensional ultrasound carotid atherosclerosis using sparse field level sets. *Med Phys*. 2013;40:1–17.

14. Říha K, Mašek J, Burget R, Beneš R, Závodná E. Novel method for localization of common carotid artery transverse section in ultrasound images using modified Viola-Jones detector. *Ultrasound Med Biol*. 2013;39:1887–1902.

15. Benes R, Karasek J, Burget R, Riha K. Automatically designed machine vision system for the localization of CCA transverse section in ultrasound images. *Comput Methods Programs Biomed*. 2013;109:92–103.

16. Lorza AM, Carvalho DD, Petersen J. Carotid artery lumen segmentation in 3D free-hand ultrasound images using surface graph cuts. Medical Image Computing and Computer-Assisted Intervention 8150 LNCS; 2013:542–549.

17. Yeom E, Nam KH, Jin C, Paeng DG, Lee SJ. 3D reconstruction of a carotid bifurcation from 2D transversal ultrasound images. *Ultrasonics*. 2014;54:2184–2192.

18. Narayan NS, Marziliano P. Echogenicity based approach to detect, segment and track the common carotid artery in 2D ultrasound images, 37th Annual International Conference of the IEEE Engineering in Medicine and Biology Society, EMBC 2015-Novem; 2015:2989–2992.

19. Smistad E, Lindseth F. Real-time automatic artery segmentation, reconstruction and registration for ultrasound-guided regional anaesthesia of the femoral nerve. *IEEE Trans Med Imaging*. 2016;35:752–761.

20. Narayan NS, Marziliano P, Kanagalingam J, Hobbs CG. Speckle patch similarity for echogenicity-based multiorgan segmentation in ultrasound images of the thyroid gland. *IEEE J Biomed Health Inform*. 2017;21:172–183.

21. Mulet-Parada M, Noble JA. 2D+T acoustic boundary detection in echocardiography. *Med Image Anal*. 2000;4:21–30.

22. Meinders JM, Brands PJ, Willigers JM, Kornet L, Hoeks APG. Assessment of the spatial homogeneity of artery dimension parameters with high frame rate 2-D B-mode. *Ultrasound Med Biol*. 2001;27:785–794.

23. Rankin N, Downey B, Munk L, Levin F. Review article sonographic reconstruction: techniques and diagnostic applications. *AJR*. 1993;161:695–702.

24. Landry A, Spence JD, Fenster A. Quantification of carotid plaque volume measurements using 3D ultrasound imaging. *Ultrasound Med Biol*. 2005;31:751–762.

25. Friedland N, Adam D. Automatic ventricular cavity boundary detection from sequential ultrasound images using simulated annealing. *IEEE Trans Med Imaging*. 1989;8:344–353.

26. Kass M. Witkin A. Terzopoulos D. Snakes: active contour models. *Int J Comput Vision*. 1988;1:321–331.

27. Gonzalez R, Woods R. *Digital Image Processing*. Upper Saddle River: Prentice-Hall; 2002:455.

28. Bridge CP. Introduction To The Monogenic Signal; 2017:1–21.

29. Kovesi P. Image Features from Phase Congruency, Videre; 1999;1:C3.

30. Otsu N. A threshold selection method from gray-level histograms. *IEEE Trans Syst Man Cybernet*. 1979;9:62–66.

31. Moerman KM. GIBBON: the geometry and image-based bioengineering add-on. *J Open Source Softw*. 2018;3:506.

32. Desbrun M, Meyer M, Schröder P, Barr AH. Implicit fairing of irregular meshes using diffusion and curvature flow. In: Proceedings of the 26th annual conference on Computer graphics and interactive techniques - SIGGRAPH '99; 1999:317–324.

33. Chalana V, Yongmin K. A methodology for evaluation of boundary detection algorithms on medical images. *IEEE Trans Med Imaging*. 1997;16:642–652.

34. Felsberg M, Sommer G. The monogenic signal. *IEEE Trans Signal Process*. 2001;49:3136–3144.

35. Fenster A, Downey DB. Three-dimensional ultrasound imaging. *Phys Med Biol*. 2001;2:457–475.

36. Lindseth F, Tangen GA, Lang∅ T, Bang J. Probe calibration for freehand 3-D ultrasound. *Ultrasound Med Biol*. 2003;29:1607–1623.

37. Chung SW, Shih CC, Huang CC. Freehand three-dimensional ultrasound imaging of carotid artery using motion tracking technology. *Ultrasonics*. 2017;74:11–20.

38. Fenster A, Downey DB. Three-dimensional ultrasound imaging and its use in quantifying organ and pathology volumes. *Anal Bioanal Chem*. 2003;377:982–989.

39. Carvalho DD, Klein S, Akkus Z, et al. Estimating 3D lumen centerlines of carotid arteries in free-hand acquisition ultrasound. *Int J Comput Assist Radiol Surg*. 2012;7:207–215.

40. Pelz JO, Weinreich A, Karlas T, Saur D. Evaluation of freehand B-Mode and power-Mode 3D ultrasound for visualisation and grading of internal carotid artery stenosis. *PLoS ONE*. 2017;12:1–11.

41. Smistad E, Løvstakken L. Vessel Detection in Ultrasound Images using Deep Convolutional Neural Networks. Deep Learning and Data Labeling for Medical Applications; 2016:30-38.